Hydrodeoxygenation and hydrocracking of solvolysed lignocellulosic biomass by oxide, reduced and sulphide form of NiMo, Ni, Mo and Pd catalysts

M. Grilc[a], B. Likozar[a,b,*], J. Levec[a,b]

[a] Laboratory of Catalysis and Chemical Reaction Engineering, National Institute of Chemistry, Hajdrihova 19, 1000 Ljubljana, Slovenia
[b] Faculty of Chemistry and Chemical Technology, University Ljubljana, Aškerčeva 5, 1000 Ljubljana, Slovenia

A B S T R A C T

Innovative second-generation biofuel was obtained by a low-temperature ultrasonic liquefaction of waste wood biomass in glycerol, diethylene glycol and *p*-toluenesulfonic acid, and its hydrotreatment in the presence of various heterogeneous catalysts and hydrogen donor solvents. Depolymerization and solubilization of cellulose, hemicellulose and lignin by using residual glycerin from biodiesel production make solvolysis process highly sustainable thermochemical biomass to liquid (BtL) route. Solvolytic oil containing 25–33 wt% of liquefied spruce and fir sawdust was upgraded by hydrotreatment utilizing heterogeneous catalysis at 300 °C and 8 MPa of hydrogen pressure. Prior to kinetic experiments, mass transfer and heat transfer resistances were reduced, and activity of catalytic hydrocracking and hydrodeoxygenation (HDO) was investigated for four NiMo/Al$_2$O$_3$ bifunctional catalysts in oxide, reduced and sulphide form, Ni/Al$_2$O$_3$–SiO$_2$, MoS$_2$, Pd/Al$_2$O$_3$ and Pd/C. Promoting effects of hydrogen donor solvents were investigated for tetralin, phenol, 2-propanol, pyridine, *m*-cresol, anthracene, cyclohexanol and xylene. Lumped reaction kinetic model was developed to determine kinetics of hydrogenolysis, decarboxylation, decarbonylation and hydrocracking of products of liquefaction, such as levulinic acid, guaiacol and hydroxymethyl furfural (HMF), according to their functional groups and related gaseous products, quantified by Fourier transform infrared spectroscopy. Upgraded liquid product was also characterized for energetic and fuel applications by following its rheological properties and measurements of gross calorific value.

© 2013 Elsevier B.V. All rights reserved.

1. Introduction

Energy requirements and environmental concerns have led to increased interest in substituting the fossil fuels with the alternatives, derived from biomass, a renewable and sustainable carbon source. The utilization of lignocellulosic waste, such as forest residues and sawdust, is especially sustainable and economically attractive, because the feedstock does not compete with food production or land use. Lignocellulosic biomass can be converted into biofuel by biochemical or thermochemical processes. The latter include technologies such as pyrolysis, gasification, supercritical fluid extraction, and direct liquefaction [1]. Traditional direct biomass liquefaction process operates at high temperature and pressure using reductive atmosphere and heterogeneous catalysts [2]. The high production costs and lack of basic scientific

understanding of the process led to the failure of relatively large demonstration plants in the late seventies [3]. Alternative direct liquefaction process is the solvolysis at mild reaction conditions, using acidified or alkaline polyhydroxy compounds as solvents [4–6]. Although the volumetric energy density of liquefied oil is significantly higher in comparison to original lignocellulosic biomass, there are main drawbacks for its direct use as a transportation fuel, e.g. the low calorific value due to high oxygen content, high viscosity, corrosive effects, and questionable chemical stability.

There are two general routes for upgrading the biomass-derived oils, namely hydrodeoxygenation (HDO) using heterogeneous catalysts and cracking with zeolites [7,8]. The catalytic HDO refers to the oxygen removal through the elimination of water, where the hydrogen content decrease in product is avoided by the high pressure of hydrogen or the presence of hydrogen donor solvent. It is an expensive, but technically and economically feasible route to convert the biomass-derived oil into transportation fuel [8]. Deoxygenation can be also achieved by CO and CO$_2$ formation; however, this route leads to lower product yields due to the depletion of carbon in liquid phase. The selectivity of deoxygenation reactions depends on the nature of feedstock, reaction conditions

* Corresponding author at: Laboratory of Catalysis and Chemical Reaction Engineering, National Institute of Chemistry, Hajdrihova 19, 1000 Ljubljana, Slovenia. Tel.: +386 1 4760283; fax: +386 1 4760300.
E-mail address: blaz.likozar@ki.si (B. Likozar).

and catalyst. The most frequently examined HDO catalysts are $NiMo/Al_2O_3$ and $CoMo/Al_2O_3$, as these are commercially used for hydrotreatment in petroleum refineries [9,10].

Sulphidation may improve their efficiency, but can be questionable in the industrial scale for the environmental reasons and sulphur compounds in product, therefore the oxide or reduced forms of these catalysts were predominantly investigated [11,12]. Nonetheless, if the activity, selectivity and stability of a sulphide form catalyst greatly surpassed the reduced equivalent, the activation procedure by sulphur-containing components would be justified even on a larger scale. Moreover, by investigating the HDO of the model compounds using these types of bifunctional catalysts, reaction pathways [13,14] and catalytic mechanisms [15] were proposed. In addition to the conventional bifunctional catalysts, catalytic upgrade was also investigated over Fe, Ni [11,16–18], and noble metals, such as Pd, Ru, Rh and Pt, on different supports [19,20].

Some results on the catalytic HDO of the biomass-derived oils liquefied at high pressures are presented in the literature [10,21,22], while the solvolysis of biomass in the acidic or alkaline polar solvents at atmospheric pressure and low temperatures, followed by catalytic upgrade, has not been extensively reported [5,11].

Hydrogen donor solvents enhance HDO by releasing the hydrogen radicals that can stabilize the free radicals, formed by the cleavage of C—O, C—N and C—C bonds, preventing the undesired reactions of charring and polymerization [23]. The effect of hydrogen donor solvents in the liquefied biomass hydrogenation process is not extensively reported as well. Tetralin is the most typical hydrogen donor solvent, used for the biomass-derived oil processing [11,22,23], while 2-propanol [24], *m*-cresol, anthracene and isoquinoline [2] were also reported to have donor effect.

In order to understand, describe and scale-up the hydrotreatment of biomass-derived oils, chemical kinetic modelling may be considered to play a crucial role in devising the activity, selectivity and stability of a catalyst. The kinetic studies of real bio-oil HDO are rare and always simplified by lumping. Zhang et al. [25] used a power law kinetic expression to evaluate the HDO of a pyrolysis oil using the CoMo catalyst in a batch reactor. Additionally, Sheu et al. [26] also used a simple power law model for the wood-derived pyrolysis oil HDO using Pt, NiMo, CoMo catalysts. The rate of oxygen removal was represented as a function of the oxygen content and partial pressure of hydrogen, while the temperature dependence of rate constant was given by the Arrhenius law.

In this work, hydrodeoxygenation of biomass, liquefied at 160 °C in acidified glycerol and ethylene glycol mixture, was carried out using 18 different catalysts and 8 hydrogen donor solvents, at the temperature of 300 °C and 8 MPa of hydrogen pressure. The influence of other parameters (i.e. temperature, pressure, process gas, heat-up rate, stirring speed, mass fraction of NiMo catalyst and

tetralin) on hydrotreatment of the same feedstock was reported in previous study [27]. The aim of this work was to determine the influence of various catalysts and donor solvents on the rate and selectivity of upgrading-associated reactions (e.g. hydrodeoxygenation, decarbonylation, decarboxylation, hydrocracking), to propose the most suitable option for a large-scale process. The novelty of this work is the advanced reaction pathway network and lumped kinetic model for the upgrading-associated reactions of the real biomass-derived oil, based on the oxygen-containing functional groups, followed by Fourier transform infrared (FTIR) spectroscopy, and their corresponding gaseous oxygen carriers. This method allows for a simple, but an advanced insight into the complex reaction system in comparison to kinetic models, based on elemental analysis.

2. Experimental

2.1. Liquefied biomass preparation and characterization

For this study, liquefied wood samples were provided by the company that runs the pilot plant for the liquefaction of the lignocellulosic biomass in polyols, following the procedure, presented in literature [28,29]. Dry sawdust from debarked European spruce (*Picea abies*) and European silver fir (*Abies alba*) was used as a feedstock, while the mixture of glycerol and diethylene glycol (1:1 by mass) was used as the liquefaction solvent, containing 3 wt% of *p*-toluenesulfonic acid as a homogeneous catalyst. The approximate mass fractions of cellulose, hemicellulose and lignin in the sample of sawdust were 41, 25, and 29%, respectively.

Two sample grades, treated in this study, consisted of the biomass to solvent ratios of 1:3 and 1:2 (by mass). The first sample had the gross calorific value (GCV) of 21.9 MJ kg^{-1}, viscosity of 4 Pa s at 25 °C, and the elemental composition as follows; 47.6 C, 8.0 H, 43.3 O, 0.2 N and 0.9 S (wt%). Water content was below 2 wt%. The second sample had the same GCV and elemental composition (within experimental error), while the viscosity at 25 °C was significantly higher (13 Pa s).

2.2. Catalyst preparation and characterization

Four types of producer-provided commercially available bifunctional nickel–molybdenum catalysts on γ-Al$_2$O$_3$ support were studied (Table 1). They were all extrudates (quadrilobe-shaped) of different dimensions, Ni and Mo content and specific surface area. In the present study each NiMo catalyst was tested in oxide/calcination-treated (as received), reduced and sulphide form.

Palladium-based catalysts, tested in this study, were supported on 2–4 mm Al$_2$O$_3$ spheres (G-68 C and G-68 G, Süd – Chemie, Munich, Germany) or on activated carbon powder (Nikki-Universal, Tokyo, Japan and Sigma–Aldrich, St. Louis, MO, USA). All

Table 1
Catalysts used for hydrotreatment process tests.

Supplier	Catalyst	Active metal	Content (wt%)	Form[a]	Pre-treatment[b]	Surface area (m^2 g^{-1})
Industrial #1	NiMo/Al$_2$O$_3$ #1	Ni/Mo	Standard/standard[c]	1.3 mm Q	O, R, TS	Standard[c]
Industrial #1	NiMo/Al$_2$O$_3$ #2	Ni/Mo	Standard/highest[c]	1.5 mm Q	O, R, TS	Standard[c]
Industrial #2	NiMo/Al$_2$O$_3$ #3	Ni/Mo	Highest/standard[c]	1.0 mm Q	O, R, TS	Highest[c]
Industrial #2	NiMo/Al$_2$O$_3$ #4	Ni/Mo	Lowest/lowest[c]	1.0 mm Q	O, R, TS	Lowest[c]
Süd–Chemie	Pd/Al$_2$O$_3$ #1	Pd	<1	2–4 mm S	R	118
Süd–Chemie	Pd/Al$_2$O$_3$ #2	Pd	<1	2–4 mm S	R	93
Sigma–Aldrich	Pd/C #1	Pd	5	P	R	1558
Nikki-Universal	Pd/C #2	Pd	5	P	R	1201
Sigma–Aldrich	Ni/SiO$_2$–Al$_2$O$_3$	Ni	65	P	R	149
Riedel de Haën	Bulk MoS$_2$	Mo	100	P	None	2

[a] Q – quadrilobe extrudates; S – spheres; P – powder.
[b] O – used as received in oxide form; R – reduced form; TS – sulphide form by TOTSUCAT process.
[c] Among industrial NiMo catalysts.

palladium catalysts, as well as the nickel catalyst on silica–alumina (65 wt% Ni, Sigma–Aldrich, St. Louis, MO, USA), were reduced prior to use, while the unsupported molybdenum disulphide powder (p.a. grade, Riedel de Haën, Seelze, Germany) was used as received.

Catalyst reduction was performed in a tube furnace. The catalysts were firstly dried under the N_2 purge (5.0 grade, Messer, Bad Soden am Taunus, Germany) at 250 °C for 60 min, consequently exposed to the H_2 flow (5.0 grade, Messer, Bad Soden am Taunus, Germany) at 150 °C for 60 min, and they were lastly heated-up (the ramp of 0.25 K min^{-1}) to 350 °C and reduced under H_2 purge for additional 7 h.

Bifunctional NiMo catalysts were sulphided off-site in the laboratory Totsucat® process by Eurecat (La Voulte-sur-Rhône, France) using H_2S/H_2 sulphiding agent. The activated catalysts only required the heating-up to the operation conditions prior to the use.

All fresh catalysts were structurally characterized after the pre-treatment by field emission scanning electron microscopy (FEG-SEM) (SUPRA 35 VP, Carl Zeiss, Jena, Germany), energy dispersive X-ray spectroscopy (EDX) (Inca 400, Oxford Instruments, Tubney Woods, UK) and the X-ray powder diffraction (XRD) analysis (D 5000, Siemens, Munich, Germany) with the CuKα radiation source (λ = 1.5406 Å) within the diffraction angle range of 10–80°. Their specific surface area was measured by BET (Brunauer–Emmett–Teller) method using the ASAP 2020 (Micrometrics, Norcross, GA, USA) instrument for gas adsorption. The sample chamber with the catalysts was evacuated at 90 °C to 6.6 Pa for 30 min and the additional 3 h at 180 °C to reach the pressure below 0.40 Pa. The adsorption isotherm was determined at −196 °C by gradually increasing the nitrogen pressure in the sample chamber (2000 Pa steps) from 6 to 30 kPa and monitoring the amount of the adsorbed nitrogen.

The temperature programmed reduction (TPR) analysis of the NiMo pellets before and after the reduction at 350 °C was conducted using Micrometrics AutoChem II Chemisorption Analyzer (Micrometrics, Norcross, GA, USA). After samples were purged with Ar at 120 °C for 1 h, they were cooled down to −15 °C and exposed to the mixture of 5 mol% H_2 in Ar. When baseline was stable, TPR analysis was started by heating-up the system to 1123 K with the heating rate of 4 K min^{-1} and by monitoring temperature and thermal conductivity detector (TCD) signal. The same apparatus and initial procedure were used to follow the progression of the isothermal reduction programme of NiMo catalysts. Calcination-treated NiMo sample was heated-up to the final temperature under the constant flow of 5 mol% H_2 in Ar (the heating rate of 10 K min^{-1}) and

maintained for 7 h, measuring the hydrogen consumption as a function of time. The weight loss of catalysts was determined as well.

2.3. Reaction mixture preparation

Before each run, the oil from solvolysis was firstly homogenized and then diluted by a hydrogen donor solvent in 3:1 (oil to solvent) mass ratio, as it is known that the higher oil to solvent ratio results in the formation of the coke during hydrotreatment [11] and re-polymerisation reactions [27]. To study the promoting effects during hydrotreatment, the following solvents were examined: tetralin (≥97 wt%, Sigma–Aldrich, [27]), phenol (≥99 wt%, Sigma–Aldrich, [27]), 2-propanol (≥99.9 wt%, Merck), pyridine (≥99 wt%, Merck, Whitehouse Station, NJ, USA), m-cresol (≥99 wt%, Merck, [27]), anthracene (≥96 wt%, Merck, [27]), cyclohexanol (≥99 wt%, Fluka, Milwaukee, WI, UAS), and xylene (≥99 wt%, Chem-Lab, Zedelgem, Belgium). The catalyst loading into solution was 7.5 wt% with respect to the primary oil of solvolysis (liquefied biomass). In catalyst screening tests, tetralin was used as the hydrogen donor solvent, while the NiMo #1 catalyst in oxidized form (Table 1) was used for the experiments with different hydrogen donor solvents.

2.4. Hydrotreatment process

The hydrotreatment of liquefied biomass was performed in the 300 mL cylindrical stainless steel reactor (Parker Autoclave Engineers, Erie, PA, USA) with the inner diameter of 43 mm and the height of 210 mm. The reactor was equipped with the magnetically driven Rushton turbine impeller with the diameter of 30 mm, located 55 mm above reactor bottom. Experimental set-up in general consisted of hydrogen cylinder, the autoclave with stirring (slurry), water-cooled condenser, temperature and gas flow regulator, and Fourier transform infrared (FTIR) spectrometer (Fig. 1).

After 200 mL of reaction mixture (primary oil, hydrogen donor solvent and catalyst) was fed into the reactor, it was attached to the casing and sealed. The air in headspace was removed by the purge of H_2, followed by pressure seal tests, and the final H_2 reaction pressure elevation up to 8 MPa. To ensure an enhanced hydrogen mass transfer and the high hydrogen availability in liquid phase and on catalyst surface, the reaction mixture under 8 MPa pressure was continuously purged with the 1.0 L_N min^{-1} flow of fresh hydrogen and was intensively stirred using the agitation speed of 1000 min^{-1}.
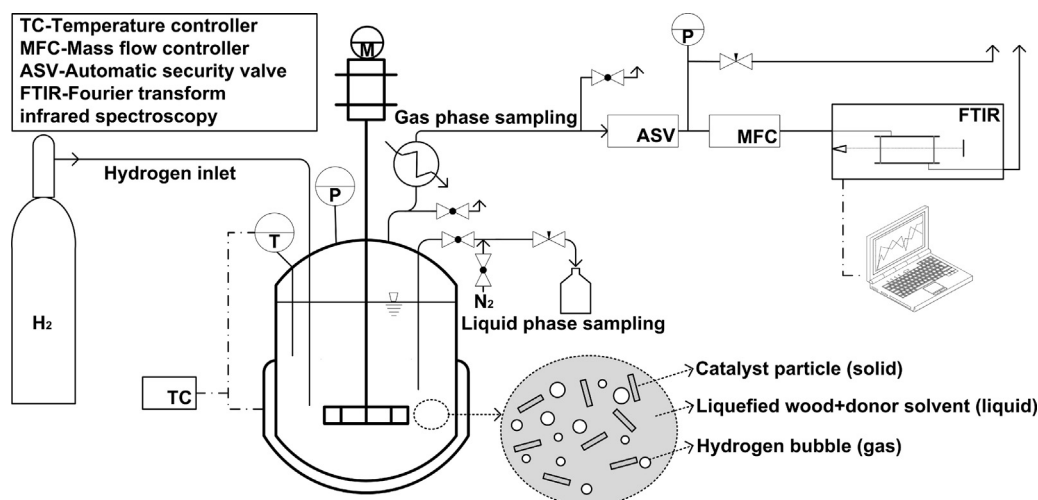

Fig. 1. Experimental set-up for hydrotreatment of liquefied lignocellulosic biomass.
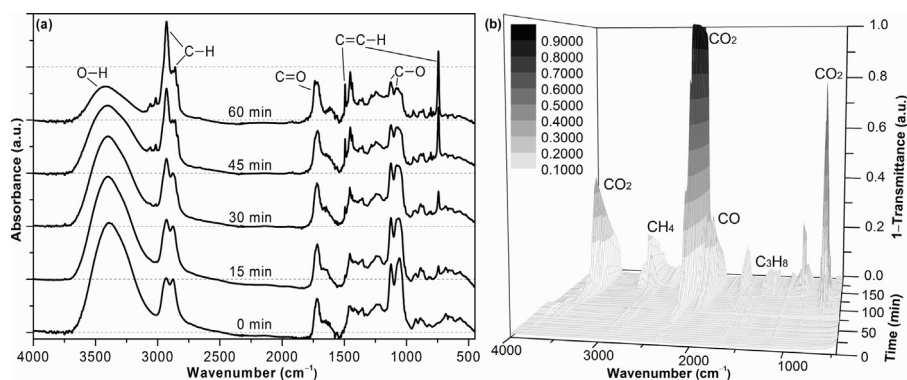
Fig. 2. FTIR spectra of liquid phase for samples collected in 15 min intervals after final temperature (300 °C) was reached (a) and 3D FTIR spectra of gas phase as a function of time (b) for hydrotreatment by using NiMo #1 catalyst without pre-treatment and tetralin as donor solvent.

Reactor content was heated from the room temperature to 300 °C by the heat-up rate of 2.5 K min^{-1} using the electric jacket heater with PID regulator (SR25, Shimaden, Tokyo, Japan). The reaction was maintained for 60 minutes at constant temperature, pressure (8 MPa), hydrogen flow rate (1.0 L$_N$ min^{-1}) and stirring speed. After 60 min, the reactor was rapidly cooled below 70 °C, while pressure was gradually released afterwards.

The catalyst particles and tar residue (not always present) from reactor vessel were separated from the liquid fraction by filtration. Tar products were not filterable without the preceding dissolution in ethanol or tetrahydrofuran. Used catalyst was washed with ethanol and dried before being structurally characterized by SEM. The volatile fraction, usually a two-phase mixture, from water-cooled condenser was also collected and weighted.

2.5. Analysis of reactants, intermediates and products

The cooled and decompressed gas phase from the reactor flew continuously through the short path gas cell with KBr windows and was analyzed online by Fourier transform infrared (FTIR) spectroscopy (Spectrum 100, Perkin Elmer, Waltham, MA, USA), once per minute. Triglycine sulphate (TGS) detector was used in mid-infrared (MIR) region to scan the spectrum in the range of 450–4000 cm^{-1}. After the FTIR response for each component i was identified and checked, whether representative absorbance ($A_{\nu,i}$) peaks were not convoluted and corresponded to Gaussian shape, they were integrated with respect to the wavenumber (ν) in interval, where peak was located, bounded by $\nu_{1,i}$ and $\nu_{2,i}$.

$$A_{\text{average},i} = \frac{1}{(\nu_{2,i} - \nu_{1,i})} \int_{\nu_{1,i}}^{\nu_{2,i}} A_{\nu,i} \, d\nu \tag{1}$$

The average absorbance value of the peak, $A_{\text{average},i}$, generally linearly corresponded to the molar fraction (x_i) of the component i in the gas cell with constant path length, l, according to the modified Beer–Lambert law.

$$A_{\text{average},i} = \varepsilon_i l x_i \tag{2}$$

To ensure higher accuracy, gas phase composition was calculated by linear interpolation using calibration data instead of the calculation from extinction coefficient, ε_i (Table SD.2.), as the correlation between absorbance peak height and molar fraction is not perfectly linear in the whole range for some components. Calibration curve was prepared by the reference gas mixtures with the known compositions of carbon monoxide, carbon dioxide, methane

and propane. After the molar fraction of the gases in the stream from reactor (Q is the volumetric flow rate at temperature T and pressure P) as a function of reaction time was known, the total amount of components (n_i), formed until time (t_{int}), was calculated by Eq. (3), where time delay between the compound formation and its actual analysis was also taken into consideration.

$$n_i(t_{\text{int}}) = \frac{PQ}{RT} \int_0^{t_{\text{int}}} x_i(t) \, dt \tag{3}$$

Baseline shift, absorbance peak integration, the molar fraction calculation by its interpolation within the range of standard data, and the calculation of the total amount of formed components was performed numerically in Matlab 7.12.0 (MathWorks, Natick, MA, USA). This methodology allowed quantifying the 6 representative absorption peaks of the 4 gases for approximately 170 different time increments per each experiment.

Six liquid samples were collected during an experiment; the first in the middle of heating period and the additional five in 15 min intervals, after the temperature of plateau was reached. The in situ monitoring of the moieties by infrared spectroscopy as a function of time, such as reported by Zakzeski et al. [30], was not realizable for our reaction system due to severe reaction conditions. To ensure the safe collection of liquid samples, sampling line consisted of three valves as shown in Fig. 1. While the valve from reactor was open for 3 s, liquid sample filled the lines between valves, and was consecutively removed by N$_2$ purge in the second step. Such configuration allowed that one valve between reactor and vial was always completely closed during sampling, and ensured the repeatability of the sampling volumes. Line plugging was not an issue; however, valves and lines were thoroughly cleaned after each run. Before each sample was collected, sampling line was flushed with about 1 g of reaction mixture. Before the FTIR analysis of liquid phase, samples were cooled and stored in the vials under nitrogen atmosphere, before they were spread over 525 μm-thick silicon wafers using the film applicator (Erichsen 360 (Hemer, Germany)) with 150 μm gap clearance (IR path length). After background was scanned using the clean and dry silicon wafer in the nitrogen-purged FTIR chamber, each sample was applied and scanned 5 times in the range of 450–4000 cm^{-1} to calculate the average measured concentration of the moieties in liquid phase, while methodology was analogous to the analysis of gas phase. The quantification of moieties is further described in Section 3.3.2 and in our previous work [27].

The gross calorific value of product was determined using the IKA C 4000 adiabatic bomb calorimeter (IKA, Staufen, Germany), following the TS CEN/TS 15400:2011 standard. An average value was calculated from 3 measurements.

3. Results and discussion

3.1. Catalyst characteristics

The characteristics of the fresh catalysts used in the HDO tests are collected in Table 1 and the SEM images of all catalyst types are depicted in Supplementary data (Fig. SD.1). NiMo/Al_2O_3 catalysts had different loadings and ratios of active metals, as well as diverse specific surface areas. During the sulphidation of catalysts, specific surface area decreased due to mass gain, as oxygen was replaced by sulphur, while surface morphology remained unchanged during the process. Reduction should have on the other hand increased the value of specific surface area, which was the case for industrial catalysts #1 and #2, while it remained nearly unchanged for industrial catalysts #3 and #4. BET measurement uncertainty could have been the reason for anomaly, but more probably the observed slight degradation of catalysts' surface morphology was responsible for observed behaviour.

In order to evaluate the extent of reduction, the temperature programmed reduction analysis (TPR) with H_2 was performed for the catalysts in oxide form and after their reduction. The typical measured TPR profile for the NiMo catalyst in oxide form (Fig. SD.2) is in accordance with the profiles, reported in the literature for NiMo catalysts, where the strong peak at 390 °C corresponds to the reduction of Ni oxide species and the partial reduction of Mo oxides, while the less observable peak at 800 °C is reported to represent the reduction of the superficially reduced Mo compounds and species exhibiting the strong interaction with support [31]. The TPR profile for reduced catalyst (Fig. SD.2) reveals that the first peak is not present; hence, corresponding oxides were successfully removed during the reduction at 350 °C. Although reduced catalyst was stored in nitrogen atmosphere, the first signs of the oxidation during the exposure of the catalyst to air were reflected as a small peak at 240 °C. The minor oxidation in air is not problematic, as formed oxides are rapidly reduced at reaction conditions (300 °C, 8 MPa of H_2). Oxides that correspond to second peak were not reduced, as the temperatures around 800 °C are required to transform all Mo species to metal form, which would result in a rather large extent of the sintering of catalyst and the degradation of its structure.

The course of the isothermal NiMo sample reduction at 350 °C for 7 h was investigated using the same apparatus as for TPR analysis, while hydrogen consumption was followed as a function of time. Fig. SD.3 shows that hydrogen consumption reached its peak 25 min after reaching 350 °C and decreased to a low but stable level in ensuing 60 min. This revealed that after 90 min the extent of reduction was very close to thermodynamic equilibrium. The hydrogen consumption after the 6 h of the reduction at 350 °C dropped below detection limit.

The mass loss after isothermal reduction test corresponded to the 64 mol% reduction of the oxygen in both Ni and Mo oxides, which is in accordance with the difference of the hydrogen consumption (67 mol%) during the TPR analysis for the NiMo in oxide and reduced form.

3.2. FTIR analysis

Fig. 2a shows the typical FTIR spectra of the liquid samples, collected in 15 minute intervals, after the temperature of plateau was reached for the run with NiMo #1 catalyst (no pre-treatment) and tetralin donor solvent. The strong broad peak at 3400 cm^{-1} represents an abundant presence of hydroxyl group at the initial stages of reactions, while the subsequent decrease during HDO reveals the significant reactivity of this group. The peak at 1721 cm^{-1} represents carbonyl, the second important oxygen-containing bonded group, which does not change much within the 60 min of hydrotreatment. The water formation in the liquid sample during heating period resulted in the appearing peak at 1650 cm^{-1}. This peak consequently decreased within reactions' time as water vapour was continuously removed from the reactor by hydrogen stream. The total pressure in reactor was indeed lower than the water vapour pressure at final temperature. The band between 2800 and 3000 cm^{-1} represents sp^3 C—H bond, where the increase of the peak at 2934 cm^{-1} can be explained with the saturation of deoxygenated or cracked sites and also by the hydrogenation of the aromatic ring donor solvent. In fingerprint region, several convoluted distinct peaks were found. Alkyl group increase can be also confirmed by the peak of the C—H deformation at 1453 cm^{-1}, while the newly-evolving peaks, found at 1497 cm^{-1} and 746 cm^{-1}, correspond to *cis*-alkene bond vibrations. Characteristic C—O deformations can be observed as convoluted characteristic peaks at 1126 and 1057 cm^{-1}. As their heights follow the behaviour of the O—H peak at 3400 cm^{-1} it can be concluded that the C—O bond in liquefied biomass is mostly present as a part of hydroxyl group.

Fig. 2b shows the FTIR spectrum of gas phase as a function of the reactions' time for the run with NiMo #1 catalyst and tetralin as donor solvent. Remarkable gas formation started after temperature exceeded approximately 275 °C, when CO_2 and CO appeared simultaneously. The characteristic absorption bands of CO were detected at 2173 and 2115 cm^{-1}, while the characteristic response of the FTIR for CO_2 could have been found in three regions; as the quartet of the peaks between 3770 and 3540 cm^{-1}, as the strong double peak at 2362–2335 cm^{-1}, and as a sharp single peak at 669 cm^{-1}. After the temperature of plateau was reached, light hydrocarbons were formed, since methane was detected as the sharp peaks at 3017 and 1304 cm^{-1} and propane presence as the broad peaks at 2968 cm^{-1} and 1471 cm^{-1}. The agreement between a given gas phase spectrum (the reduced NiMo #3 catalyst at 140 min) and the spectra of the pure CO_2, CO, CH_4, or C_3H_8 in nitrogen is shown in Supplementary data (Fig. SD.4). All major gas phase bands were identified and quantified with the latter gaseous compounds, except for the two minor peaks within 1800–1620 cm^{-1} that represented a minor presence of volatile carbonyl compounds and a sharp 1050–850 cm^{-1} band that indicated the traces of light alkenes (e.g. ethylene).

3.3. Catalyst screening

The mixture from reactor, after being cooled to room temperature, consisted of solid catalyst particles, dark brown liquid phase, and in some cases, tarry residue. Fig. 3 shows the great influence of the catalyst type on the composition of reaction products and the calorific value of liquid phase, indicating catalysts' different activity and selectivity at 300 °C and 8 MPa H_2. Liquid phase was homogeneous, as different phases have not separated in separatory funnel. Its viscosity and gross calorific value greatly depended on the nature of catalyst. Tar residue appeared basically the same for all runs, in which it was present. It was solid at ambient temperature, melted at 40 °C, and was free-flowing at 70 °C, and had the GCV of 27.0 ± 0.8 MJ kg^{-1}. The fraction from water-cooled condenser consisted of two phases. The major part of condensed fraction (more than 85 wt%) represented aqueous phase, containing the water from HDO, since the pressure in reactor was set slightly below the vapour pressure of water (8.6 MPa) at reaction temperature; hence, it was continuously removed from the reactor vessel by the purge of gaseous phase. The FTIR spectrum of water concealed other possible compounds or functional groups, present in aqueous phase, and GCV was below reliable detection limit. Light hydrocarbons (deoxygenated) represented only a minor part of the condensed fraction (below 15 wt%) with the GCV over 39 MJ kg^{-1}.

The closure of the mass balance in terms of separated products (e.g. a certain portion of products was attached to apparatus)
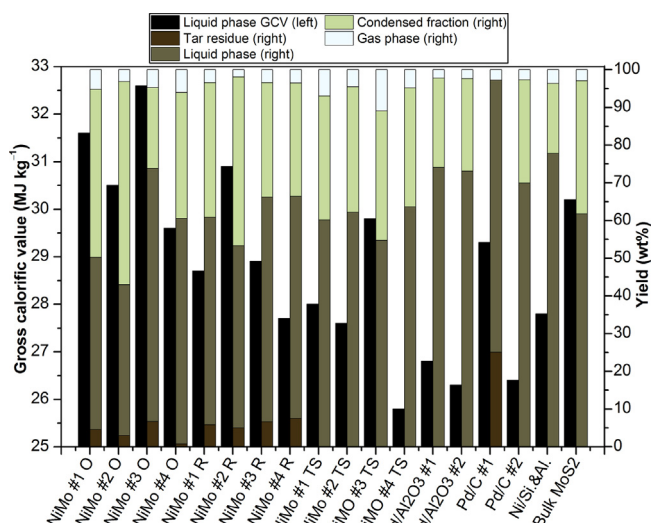
Fig. 3. Gross calorific value of final liquid phase and mass balances of reaction products using different catalysts and pre-treatments for hydrotreatment of liquefied lignocellulosic biomass (300 °C, 8 MPa H₂, 1 h).

varied for different catalysts, as it generally reflected the viscosity of product and especially the formation of tar residue. For some experiments, the closure of mass balance was below 85 wt%, due to the high viscosity of liquid product that wrapped stirrer, lining and reactor wall (predominant factor). The mass of gas phase may also contribute to the losses in mass balance, as only the amounts of gases, quantified by FTIR, were considered, while some minor peaks from gas sample spectrum were not quantified (Fig. SD.4).

Among NiMo/Al₂O₃ catalysts, the utilization of oxidized form resulted in the highest calorific value of liquid phase, but also in its high viscosity and correlated tendency to stick on reactor walls, impeller and tubing, also leading to slightly poorer mass balance agreement. The oxide form of NiMo #1 was also utilized for the hydrotreatment of the solvolytic primary oil, prepared form the 1:2 lignocellulosic biomass to solvent ratio (instead of the mass ratio of 1:3), which resulted in very similar product distribution, while the GCV of liquid phase was slightly lower (30.5 MJ kg⁻¹). NiMo #3 exhibited the best catalytic performance among oxidized NiMo catalysts, regarding calorific value as well as the yield of liquid phase. This is expected as its specific surface area is more than 30% higher in comparison to any other NiMo catalyst used, beside Mo and Ni contents also being among the highest (Table 1). Pre-reduction of NiMo catalysts resulted in even higher viscosity of the liquid product with lower calorific value and a higher amount of tar residue.

The use of sulphide-form NiMo catalysts led to completely different products in comparison to the most of other examined catalyst types. The enhanced (hydro)cracking activity of this catalyst converted the most of the primary oil into the liquid product with very low viscosity. When centrifugation was applied, three phases were separated; the oil phase on top, the yellow to orange aqueous phase in the middle, and a small amount of the dense unreacted liquefied biomass on the bottom. The FTIR spectra and gross calorific values of individual separated phase were alike for all runs using sulphide-form catalysts, while different ratios of phases determined the overall GCV of liquid product. The upper non-polar phase had the GCV of 36.3 ± 0.5 MJ kg⁻¹ and its residual chemically bonded oxygen was generally in carbonyl form (Fig. SD.5). Polar aqueous phase had the GCV of 13 ± 1 MJ kg⁻¹, due to abundant hydroxyl group presence. During catalytic hydrotreatment process experiments, oxygenated polar compounds were gradually transformed into less polar deoxygenated product, co-producing

water, which evaporated and was gradually removed from the reactor vessel by the stream of gas phase. The specific surface area of sulphide-form catalyst and its metal loading directly influenced catalyst performance; regarding the oil to aqueous phase ratio and the GCV of the overall liquid phase, the observed order was NiMo TS #3 > #2 ≈ #1 > #4. With respect to aqueous phase GCV, the order was reversed (NiMo TS #4 > #1 ≈ #2 > #3), so that the aqueous phase was calorically impoverished, when more active catalysts were used, hence more polar oxygenate compounds were transformed into non-polar deoxygenated products.

Nickel on silica–alumina support showed strong decarboxylation and hydrocracking activity (Fig. SD.6), which is described in detail in Section 3.3.3. The use of bulk MoS₂ catalyst resulted in a high yield of the liquid product with relatively high GCV.

The activity and selectivity of palladium-based catalysts varied regarding support and catalyst producer. The utilization of both Pd/Al₂O₃ catalysts resulted in the liquid product with low viscosity and calorific value. On the other hand, the use of Pd/C #1 yielded viscous product, high tar residue content, while no condensed fraction was formed. However, the GCV of liquid phase was relatively high. As a comparison, powder Pd/C #2 catalyst with the same metal loading and comparable specific surface area was tested, resulting in very similar results as in the case of Pd/Al₂O₃ use. The reasons for the different activities of Pd/C catalysts could be found in the dissimilar morphology of carbon support, but particularly in Pd particle-size distribution. From SEM images (Fig. SD.1f and g) it can be seen that palladium (bright spots) is evenly distributed over the support surface for Pd/C #2, and the particle sizes of Pd are largely in the range of 20 nm, while a few larger agglomerates rarely exceed 100 nm. The particles of about 20 nm are also dispersed on Pd/C #1 surface, but on the other hand, Pd agglomerates are visible, which are significantly larger and often exceed the size of 1 μm, resulting in a much lower surface area of active metal, and consequently, less active sites for the same mass of applied Pd. Although Pd contents are the same for both catalysts, and the specific surface area of Pd/C #1 support is a bit higher, the presence of large Pd agglomerates consequences in a portion of unutilized bulk mass and proportionally lowers catalytic activity.

XRD analysis showed the peaks at the 2θ values of 38.3°, 44.7°, 64.9° and 78.2° for both catalysts that can be referred to the diffraction of (1 1 1), (2 0 0), (2 2 0) and (3 1 1) Pd planes, in the same order (Fig. SD 7). For both catalysts, (3 1 1) structure is predominant, while the presence of (1 1 1) and (2 0 0) phases is significantly higher for the Pd/C #2 in comparison to Pd/C #1, while peak, that corresponds to (2 2 0) plane, is much lower. Crystallite sizes, calculated according to the Scherrer equation, were similar for all phases and for both catalysts, and amounted to 24 ± 3 nm. The different phase distribution and agglomerate formation for Pd/C #1 catalyst, alongside with the different morphology of active carbon support, are probably the main contributions to different catalytic activity, although they do not differ regarding crystallite sizes and Pd mass fractions, in comparison to Pd/C #2.

3.3.1. Reaction scheme development

The identification and quantification of all the components, present in liquefied biomass, and the further development of reaction network and the determination of kinetic parameters considering all these components would be quite unmanageable. Alternatively, the chemical species with similar chemical reactivity can be grouped into pseudo-species, the so-called lumps. The kinetics of their chemical transformation has proven to be a practical way for the kinetic modelling of multicomponent mixtures and has been traditionally used in the petroleum industry for various processes, especially for hydrocracking reactions. Instead of following the compounds "species by species" by gas chromatography, mass spectroscopy or nuclear magnetic resonance, the methods often
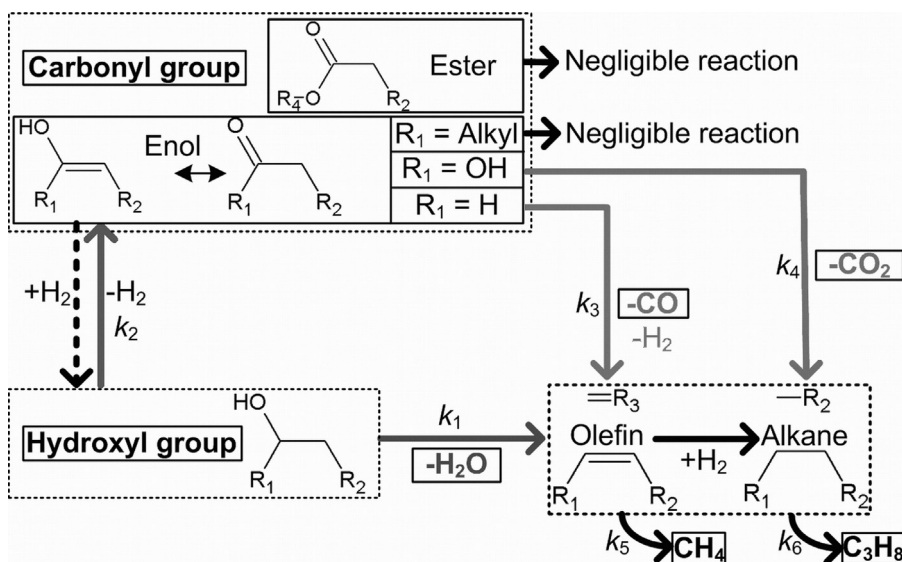
Fig. 4. Proposed reaction mechanism for deoxygenation and cracking over examined heterogeneous catalysts.

used to analyze complex mixtures such as pyrolysis oil [32], FTIR was selected as a more suitable analytical method for the lumped kinetics model in this study. Kinetics was developed with respect to two most present oxygenated groups, namely hydroxyl and carbonyl group, and their related products, H_2O, CO and CO_2. The light hydrocarbon formation with hydrocracking reactions, namely methane and propane, were also included in the model.

It is well known that hydroxyl group can be effectively deoxygenated using the $NiMo/Al_2O_3$ or noble metal catalysts on different supports in two-step catalytic reaction (hydrodeoxygenation), through the dehydration to an olefin, followed by the rapid hydrogenation to an alkane [33–35]. Secondary hydroxyl group is very selectively deoxygenated to the corresponding alkane by the latter mechanism [14], while the primary hydroxyl group can also be dehydrogenated to aldehyde, the main precursor for decarbonylation [33,35] and even disproportionation, followed by the decarboxylation reactions by direct C—C bond cleavage [34], resulting in a shorter alkane.

Ketones can also be formed by the same mechanism that is the dehydrogenation from secondary hydroxyl group, but cannot undergo decarbonylation or decarboxylation and can only be hydrogenated back to corresponding hydroxyl group, so that negligible concentrations of ketones were normally found for the HDO of primary alcohols [14,35]. Donnis et al. explain the hydroxyl to carbonyl dehydrogenation with carbonyl compound being the tautomer of enol form, which is a reactive intermediate [14], so the reversible reaction between hydroxyl and carbonyl group is assumed, where hydrogen is required to convert carbonyl to hydroxyl group, and is formed in reverse process, respectively. High hydrogen pressure shifts the equilibrium towards carbonyl hydrogenation, so the presence of the newly formed carbonyls in reaction mixture is low, but sufficient for a considerable extent of decarbonylation or decarboxylation. In contrast, the absence of hydrogen shifts the equilibrium towards the dehydrogenation of hydroxyl group, and leads to excessive CO and CO_2 formation, but still without appreciable carbonyl intermediates being detected in liquid phase [34], which indicates their high reactivity.

The carbonyl group in the acidified polyols-based primary oil can be observed as the strong peak at $1721\,cm^{-1}$ in FTIR spectrum and is generally represented by ester groups [36,37]. Esters are not known to be reactive at mild conditions of hydrotreatment, especially not for direct decarbonylation or decarboxylation reactions

due to these groups being difficultly accessible reaction sites. That was also the case in the present reaction system, where the height of the peak at $1721\,cm^{-1}$ remained more or less unchanged during hydrotreatment, reflecting the low reactivity of ester group. Furthermore, CO and CO_2 formation rates were not a function of the latter peak intensity, but corresponded to OH group concentration according to the previously described reaction mechanism. Obviously, the presence of the precursors of decarbonylation and decarboxylation was negligible in initial mixture, as they were gradually formed from the hydroxyl group, which was the rate-determining step, while C—C bond cleavage, resulting in CO and CO_2 formation, was relatively fast. Newly formed aldehydes can also react with water to form diols and are detected as the hydroxyl group in the mixture by FTIR, but nonetheless, react as aldehydes.

A significant water formation alongside with hydroxyl group disappearance indicated that water was the main oxygen carrier and the dehydration with subsequent hydrogenation was the main deoxygenating reaction pathway. Fig. 4 presents the proposed mechanism of hydrotreatment, where hydroxyl group, carbonyl group, CO_2, CO, and water are the lumps containing oxygen, involved in deoxygenation reactions, while CH_4 and C_3H_8 formation originates from hydrocracking reactions.

3.3.2. Reaction kinetics development

The influences of the different catalysts and their pre-treatment on the main reactions of oxygen removal were further explored by developing kinetic model. Modelling was performed in Matlab 7.12.0. For optimization purposes, both simplex and non-linear least squares approximation search methods were used to determine the kinetic parameters E_{an} and A_n for each reaction, the parameters corresponding to the minimum of the function, given by Eq. (4).

$$f(Ea1, A1, Ea2, A2, \ldots, Ean, An)$$
$$= \sum_{j=1}^{J} \sum_{i=1}^{I} (y_{i,j}^{meas} - y_{i,j}^{calc}(Ea1, A1, Ea2, A2, \ldots, Ean, An))^2 \quad (4)$$

i represents the index of a reaction or a corresponding lump (I is their number), and j stands for the index of an experiment using individual catalyst (J is their number), $y_{i,j}$ for the relative concentration of the lump i in the experiment j. E_{an} represents the

activation energy, and A_n the pre-exponential factor of reaction n. Superscripts *meas* and *calc* refer to the measured and calculated values. 49 combinations of activation energy values were tried as initial approximations according to the Box–Behnken design for the 6 variables in the range of values reported in literature (50–110 kJ mol^{-1}) [9,10,25,26] to ensure the convergence to global minimum, and not merely the local ones.

The values of the relative concentrations ($y_{i,j}^{calc}$) during reactions' time were determined by solving the set of differential mass balances, formulated according to reaction scheme (Fig. 4), involving 7 lump components and 6 chemical reactions. The set of differential equations was solved using the explicit Runge–Kutta ((4) and (5)) formula. In literature, mainly apparent power law rate equations were used for the modelling of hydrodeoxygenation, where reaction rate was a function of kinetic constant and the order for overall oxygen content. In this study, the apparent rate (r_n) for deoxygenation and dehydrogenation reactions (n = 1–4) was set to be dependent on the concentration of the main oxygenated functional groups in the liquid phase with the reaction order of unity. External mass transfer resistance was eliminated by the intensive stirring and continuous flow of the fresh hydrogen at 8 MPa. Internal mass transfer limitations were implicitly incorporated in kinetic rate constants (k_n), which actually represent the product of intrinsic rate constant and effectiveness factor.

$$r_n = k_n y_i \tag{5}$$

$$y_i = \frac{C_i}{C_{OH}}(t = 0) \tag{6}$$

Sheu et al. [26] also took into consideration the contribution of the reaction pressure (hydrogen) between 5 and 10 MPa on the total rate of oxygen removal; however, its reaction order was always lower than 0.31 when the sulphide-form NiMo catalyst was used. In this study, the contribution of hydrogen was not investigated, as all the experiments were done under the same pressure, while the constant purge of the fresh hydrogen at a relatively high pressure assured the sufficient and permanent hydrogen availability for HDO. However, the concentration of dissolved hydrogen may be considered to be included in corresponding rate constants.

The orders of hydrocracking apparent rates (n = 5, 6) were set to zero, which is a common practice in the cracking kinetics modelling over NiMo/Al$_2$O$_3$ [38], and in agreement with our experimental observations.

$$r_n = k_n \tag{7}$$

The balances for each lump are as follows.

$$\frac{dy_{OH}}{dt} = -k_1 y_{OH} - k_2 y_{OH} - k_4 y_{CHO} \tag{8}$$

$$\frac{dy_{C=O\,tot}}{dt} = k_2 y_{OH} - k_3 y_{CHO} - k_4 y_{CHO} \tag{9}$$

$$\frac{dy_{CHO}}{dt} = k_2 y_{OH} - k_3 y_{CHO} - k_4 y_{CHO} \tag{10}$$

$$\frac{dy_{CO}}{dt} = k_3 y_{CHO} \tag{11}$$

$$\frac{dy_{CO_2}}{dt} = k_4 y_{CHO} \tag{12}$$

$$\frac{dy_{H_2O}}{dt} = k_1 y_{OH} \tag{13}$$

$$\frac{dy_{CH_4}}{dt} = k_5 \tag{14}$$

$$\frac{dy_{C_3H_8}}{dt} = k_6 \tag{15}$$

The concentration of carbonyl groups consisted of aldehyde and ester group concentrations.

$$y_{C=O\,tot} = y_{CHO} + y_{C=O\,ester} \tag{16}$$

As mentioned before, the reactivity of ester group could be considered to be negligible.

$$\frac{dy_{C=O\,ester}}{dt} = 0 \tag{17}$$

Apparent rate constants were considered temperature-dependent according to the Arrhenius equation (R is the gas constant).

$$k_n(T(t)) = A_n \exp\left(-\frac{E_{an}}{(R \cdot T(t))}\right) \tag{18}$$

At each time increment, all apparent rate constants were calculated taking into account the corresponding temperature. The linearly interpolated values of measured temperatures were used in the model to consider the overshooting of temperature and other particularities of the temperature regime for each individual experiment, although temperature (T) generally followed the regime set (h is the heat-up rate) over time (t) by controller (Eq. (19)).

$$T(t) = T(t = 0) + ht \quad \forall T \leq T_{final} \tag{19}$$

To evaluate the initial content of the hydroxyl and carbonyl group in liquid phase, various mixtures of model compounds were prepared from the pure solvents for liquefaction (glycerol, diethylene glycol, etc.) and wood liquefaction product representatives (levulinic acid, guayacol, etc.). Mixtures were scanned by FTIR and compared with the spectrum of the initial reaction mixture until an adequate agreement was achieved (Fig. SD.8), which enabled to determine the amount of the bonded group or chemical compound per the mass of the primary oil (P.O.) in a reaction mixture (analogue to hydroxyl value). Such definition proved to be appropriate, as reaction mechanism was focused on the oxygen-containing species transformation, and these lumps could have only originated from primary oil and not hydrogen donor solvent [39] or catalyst. The following compositions of liquid and gas phases were used as the initial values in the model.

$$C_{OH}(t = 0) = 24 \pm 2 \, \text{mmol} \, g_{P.O.}^{-1}$$

$$C_{C=O\,tot}(t = 0) = 1.9 \pm 0.3 \, \text{mmol} \, g_{P.O.}^{-1}$$

$$C_{CHO}(t = 0) = 0 \, \text{mmol} \, g_{P.O.}^{-1}$$

$$C_{CO}(t = 0) = 0 \, \text{mmol} \, g_{P.O.}^{-1}$$

$$C_{CO_2}(t = 0) = 0 \, \text{mmol} \, g_{P.O.}^{-1} \tag{20}$$

$$C_{H_2O}(t = 0) = 1.1 \pm 0.1 \, \text{mmol} \, g_{P.O.}^{-1}$$

$$C_{CH_4}(t = 0) = 0 \, \text{mmol} \, g_{P.O.}^{-1}$$

$$C_{C_3H_8}(t = 0) = 0 \, \text{mmol} \, g_{P.O.}^{-1}$$

3.3.3. Modelling results

For each catalyst type, parameter estimation was performed by fitting over 650 experimental points. The model encompassed the whole temperature range including initial heating-up and not only the isothermal segment of the process at final temperature, which represented only one-third of reaction time due to relatively long heating time. The reaction behaviour during the heating-up period was described according to the Arrhenius law, where activation energies and pre-exponential factors were determined by the model and are collected in Table SD.1. The calculated rate constants

Table 2
Calculated kinetic rate constants at 300 °C for deoxygenation of liquefied biomass.

Catalyst[a]	k_1 (min^{-1})	k_2 (min^{-1})	k_3 (min^{-1})	k_4 (min^{-1})	k_5 (min^{-1})[b]	k_6 (min^{-1})[c]
NiMo #1 O	1.02×10^{-2}	1.16×10^{-3}	9.96×10^{-2}	1.65×10^{-1}	7.05×10^{-6}	2.51×10^{-5}
NiMo #2 O	1.20×10^{-2}	1.99×10^{-3}	1.02×10^{-1}	1.49×10^{-1}	9.65×10^{-6}	2.42×10^{-5}
Reused NiMo #2 O	1.47×10^{-2}	1.64×10^{-3}	9.82×10^{-2}	1.80×10^{-1}	1.29×10^{-5}	3.51×10^{-5}
NiMo #3 O	6.47×10^{-3}	1.56×10^{-3}	1.12×10^{-1}	2.84×10^{-1}	1.49×10^{-5}	5.19×10^{-5}
NiMo #4 O	8.88×10^{-3}	1.63×10^{-3}	1.43×10^{-1}	2.44×10^{-1}	1.99×10^{-5}	5.60×10^{-5}
NiMo #1 R	6.40×10^{-3}	9.26×10^{-4}	4.45×10^{-2}	8.30×10^{-2}	1.57×10^{-5}	8.46×10^{-5}
NiMo #2 R	1.47×10^{-3}	6.78×10^{-4}	7.66×10^{-1}	6.45×10^{-1}	9.57×10^{-6}	1.20×10^{-4}
NiMo #3 R	4.79×10^{-3}	7.52×10^{-4}	1.15×10^{-1}	4.09×10^{-1}	8.50×10^{-5}	8.55×10^{-5}
NiMo #4 R	9.40×10^{-3}	8.25×10^{-4}	1.51×10^{-1}	2.32×10^{-1}	1.54×10^{-5}	9.46×10^{-5}
NiMo #1 TS	3.33×10^{-2}	7.34×10^{-4}	6.41×10^{-2}	1.37×10^{-1}	9.48×10^{-5}	7.09×10^{-4}
NiMo #2 TS	3.38×10^{-2}	8.47×10^{-4}	2.26×10^{-1}	1.03×10^{-1}	9.15×10^{-5}	7.72×10^{-4}
NiMo #3 TS	2.68×10^{-2}	1.14×10^{-3}	4.58×10^{-2}	2.34×10^{-1}	1.22×10^{-4}	9.29×10^{-4}
NiMo #4 TS	2.42×10^{-2}	7.91×10^{-4}	6.39×10^{-2}	3.23×10^{-1}	8.64×10^{-5}	6.51×10^{-4}
Pd/Al$_2$O$_3$ #1	5.82×10^{-3}	8.19×10^{-4}	4.80×10^{-2}	4.69×10^{-2}	1.10×10^{-5}	3.46×10^{-5}
Pd/Al$_2$O$_3$ #2	5.81×10^{-3}	6.72×10^{-4}	6.25×10^{-2}	5.46×10^{-2}	1.19×10^{-5}	3.66×10^{-5}
Pd/C #1	7.96×10^{-3}	7.49×10^{-4}	2.07×10^{-1}	9.06×10^{-2}	1.19×10^{-5}	3.66×10^{-5}
Pd/C #2	7.24×10^{-3}	6.67×10^{-4}	1.41×10^{-1}	1.62×10^{-1}	2.66×10^{-5}	2.00×10^{-4}
Ni/SiO$_2$–Al$_2$O$_3$	9.41×10^{-3}	4.28×10^{-4}	2.29×10^{-1}	4.63×10^{-1}	1.37×10^{-4}	1.27×10^{-4}
Bulk MoS$_2$	1.31×10^{-2}	9.14×10^{-4}	4.65×10^{-2}	6.11×10^{-2}	1.27×10^{-5}	3.10×10^{-5}

[a] O – used as received in oxide form; R – reduced form; TS – sulphide form by TOTSUCAT process.

[b] actual unit of rate constant is mol$_{CH4}$ mol$_{OH}$$^{-1}$ min^{-1}.

[c] actual unit of rate constant is mol$_{C3H8}$ mol$_{OH}$$^{-1}$ min^{-1}.

for isothermal regime at final temperature (300 °C) are collected in Table 2.

Fig. 5 shows the influence of the nickel–molybdenum type of the catalysts on the progression of the bonded oxygen removal from the hydroxyl and carbonyl group through hydrogenolysis, decarbonylation and decarboxylation, and additionally, via hydrocracking reactions, followed through the formation of methane and propane. The effect of the pre-treatment of NiMo/Al$_2$O$_3$ on activity and selectivity is depicted in Fig. 5a, c, and d. The catalyst in oxide form (Fig. 5a) showed the highest activity of the decarbonylation and decarboxylation among all the catalysts tested. CO$_2$/CO molar ratio was approximately 2:1. Hydroxyl group conversion was high and the rate of (hydro)cracking reactions negligible, which is in accordance with the high calorific value and high viscosity of liquid product. Reuse of this catalyst (Fig. 5b) shows only a slight extent of the deactivation of the catalyst for decarboxylation reactions, while final hydroxyl group conversion remained unchanged, as well as the gross calorific value of liquid product. According to this results and characterization of used NiMo/Al$_2$O$_3$ (SEM, EDX, total organic carbon deposition) from the previous study [27], it can be concluded that catalyst can be reused as it predominantly retains activity and selectivity even without the cleaning or regeneration of catalyst.

Reduced-form catalyst (Fig. 5c) exhibited a similar final conversion of hydroxyl group, revealing that the reduced form of NiMo #2 catalyst possessed a similar activity of deoxygenation in comparison to an oxide, while decarbonylation and decarboxylation reactions were strongly inhibited, and CO and CO$_2$ formation was nearly equimolar. Among NiMo, deoxygenation reactions were the slowest for reduced form, while the high viscosity of product also indicated only an insignificant presence of hydrocracking reactions. The sulphidation of catalyst on the other hand strongly enhanced hydrocracking reactions, whereas hydroxyl group removal was faster as well and started at a lower temperature in comparison to reduced and oxide form. Decarboxylation has analogously already commenced at a slightly lower temperature with regard to oxide and reduced form, while decarbonylation was completely inhibited. It is interesting that the sulphidation of active metals increased the apparent rates of the cracking for nearly a factor of ten without modifying the composition and acidity of support. Nickel on silica–alumina (Fig. 5e) significantly lowered the activation energies of decarboxylation and hydrocracking reaction, as CO$_2$

formation was detected at the temperatures as low as 150 °C, and the formation of propane at 225 °C. Much lower activation energy, required for C—C bond cleavage, can be explained by a higher acidity of silica-containing support, and therefore a higher activity for fluid catalytic cracking reactions. Hydroxyl group conversion was much lower in comparison to any catalyst that contained molybdenum, which confirms its necessity as the active phase of the catalysts for required HDO activity.

Bulk molybdenum sulphide on the other hand resulted in relatively high hydroxyl group conversion achieved by a very high selectivity towards hydrodeoxygenation, and the inhibited activity for decarbonylation, decarboxylation and hydrocracking, which also resulted in a high yield of liquid phase (Fig. 3). This is in accordance with Brimont et al. [40] who reported very selective hydrogenolysis reactions over bulk MoS$_2$. The doping with nickel sacrifices this high selectivity towards hydrodeoxygenation, but improves the overall activity for deoxygenating. Fluid cracking activity was the lowest among catalysts, tested in this study, which reflects the absence of the support with acidic sites that would catalyze C—C bond cleavage.

Fig. 6 shows the results of the hydrotreatment for the palladium-based catalysts on alumina and carbon support. A significantly lower conversion of hydroxyl group was detected in comparison to the nickel and molybdenum type of catalysts, which was the main reason for the lower GCV of liquid product. All palladium-based catalysts except Pd/C #1 (presumably, owing to the uneven distribution of Pd, as detaily described in Section 3.3, resulting in the predomination of the thermal decomposition over the catalytic reactions on Pd active sites) showed the formation of CO and CO$_2$, which was nearly equimolar, and generally, a low activity for hydrocracking was observed, where carbon support use resulted in a slightly higher activity in comparison to alumina.

The summary of catalyst screening study is presented in Table 3 that shows the influence of the active phase, support, and the dispersion of the active phase on the selectivity towards deoxygenation and fluid catalytic cracking reactions. Hydrodeoxygenation and decarboxylation are desired as they increase the calorific value of product and simultaneously do not shift the mass balance in favour of the depletion of liquid product, which is the case for undesired decarbonylation reactions. The viscosity and yield of liquid phase are also given descriptively. It can be concluded from Table 3 and from previous discussion, that catalysts,
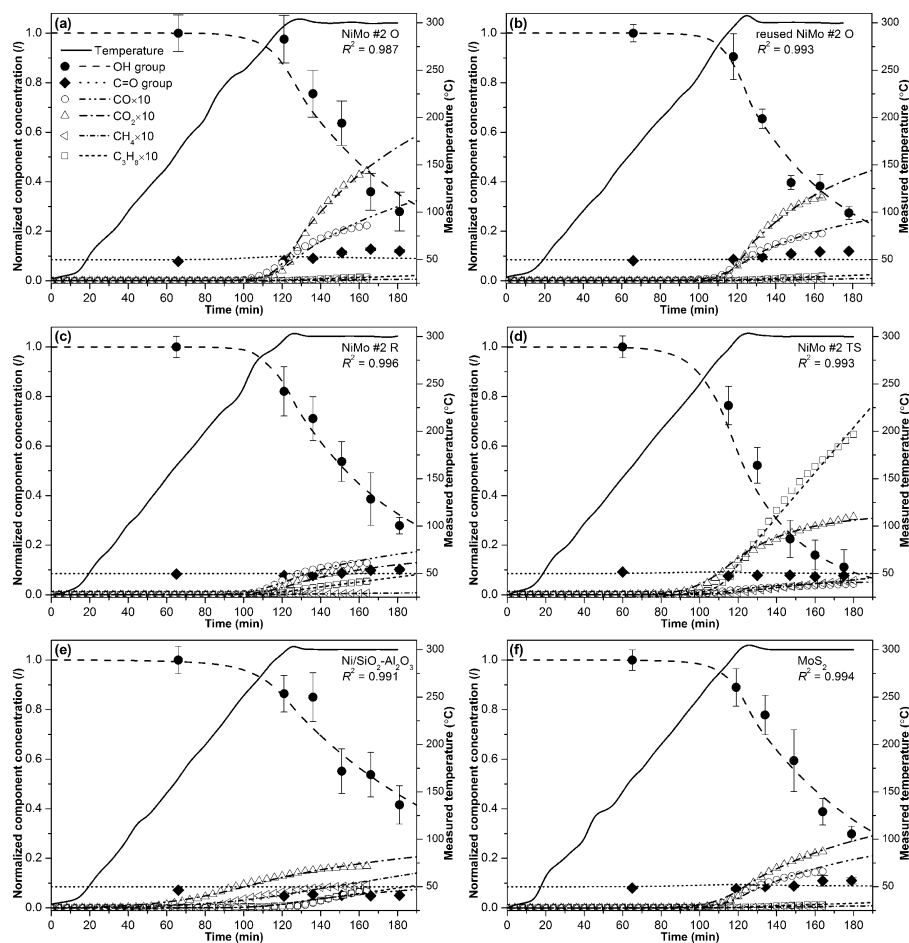
Fig. 5. Experimental (symbols) and modelling (lines) results of hydrotreatment using nickel- and molybdenum-based catalysts: NiMo #2 in oxide form (a) that was also reused without additional cleaning (b), reduced NiMo #2 (c), sulphide-form NiMo #2 (d), Ni/SiO$_2$–Al$_2$O$_3$ (e), and bulk MoS$_2$ (f); all experiments were performed at the same conditions: temperature of 300 °C, heat-up rate of 2.5 K min^{-1}, total pressure of 8 MPa, stirring speed of 1000 min^{-1}, 25 wt% of tetralin per mass of liquid phase, and 7.5 wt% of catalyst per mass of primary oil; values of normalized gas concentrations (CO$_2$, CO, CH$_4$ and C$_3$H$_8$) have been multiplied by factor of 10 to grant better clarity in given scale; legend in Fig. 5a refers to all subfigures.
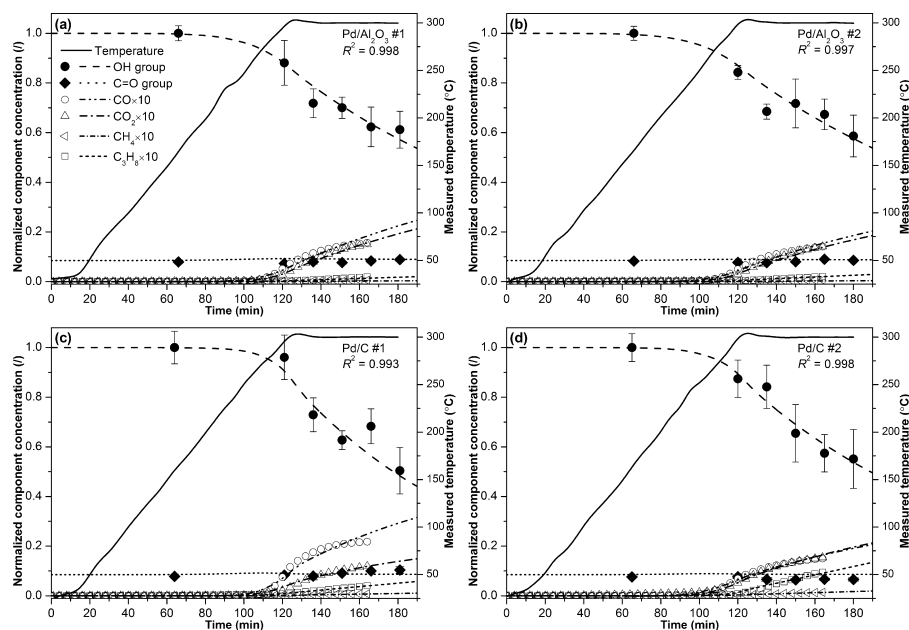

Fig. 6. Experimental (symbols) and modelling (lines) results of hydrotreatment using reduced palladium-based catalysts: Pd/Al$_2$O$_3$ #1 (a), Pd/Al$_2$O$_3$ #2 (b), Pd/C #1 (c), and Pd/C (d); all experiments were performed at the same conditions: temperature of 300 °C, heat-up rate of 2.5 K min^{-1}, total pressure of 8 MPa, stirring speed of 1000 min^{-1}, 25 wt% of tetralin per mass of liquid phase, and 7.5 wt% of catalyst per mass of primary oil; values of normalized gas concentrations (CO$_2$, CO, CH$_4$ and C$_3$H$_8$) have been multiplied by factor of 10 to grant better clarity in given scale; legend in Fig. 6a refers to all subfigures.

Table 3
Effect of catalysts' active phase and support on selectivity of hydrodeoxygenation (HDO), decarbonylation (DCN), decarboxylation (DCX) and fluid catalytic cracking (FCC) reactions, viscosity (Visc) and yield of liquid product; bold features represent favourable characteristics.

Catalyst group	Active phase	Support (acidity)	HDO	DCN	DCX	FCC	Visc.	Yield
Oxide NiMo	NiO, MoO$_3$	Al$_2$O$_3$ (medium)	**High**	High	**High**	Low	High	Low
Reduced NiMo	Ni, Mo, MoO$_2$	Al$_2$O$_3$ (medium)	**High**	**Low**	Low	Low	High	Low
Sulphide NiMo	NiS, MoS$_2$	Al$_2$O$_3$ (medium)	**High**	**Low**	**High**	**High**	**Low**	Med.
Ni/Al$_2$O$_3$–SiO$_2$	Ni	Al$_2$O$_3$–SiO$_2$ (high)	Med.	**Low**	Med.	Med.	**Low**	Med.
Pd/Al$_2$O$_3$	Pd	Al$_2$O$_3$ (medium)	Low	**Low**	Low	Low	**Low**	**High**
Pd/C #1	Pd[a]	C (neutral)	Med	Med.	Low	Low	Med.	**High**
Pd/C #2	Pd[b]	C (neutral)	Low	**Low**	Low	Med.	Med.	Med.
Bulk MoS$_2$	MoS$_2$	–	**High**	Med.	Med.	Low	Med.	Med.

[a] Pd with (3 1 1) and (2 2 0) predominating crystal planes; larger agglomerates.
[b] Pd with (3 1 1), (2 0 0) and (1 1 1) predominating crystal planes; fine dispersion, no larger agglomerates.

based on Ni and Mo, possess a higher activity for all investigated reactions in comparison to Pd catalysts. All forms of NiMo catalyst showed high HDO activity; however, active phase types have a significant influence on side reactions that importantly influenced the properties and yield of liquid product. Sulphided NiMo catalysts showed the most suitable catalytic properties by promoting (hydro)cracking, decarboxylation and HDO reactions, while simultaneously inhibiting decarbonylation. This resulted in the liquid product with low viscosity, separated phases, while still achieving relatively high yields.

To further investigate the influence of the metal loading and specific surface area for the sulphide-form NiMo/Al$_2$O$_3$ catalyst on activity and selectivity, all NiMo catalysts were also tested at the heat-up rate of 7.5 K min^{-1}. Higher heat-up rate was selected to evaluate its influence on the course of proposed reactions and potential re-polymerisation reactions, and to evaluate the necessity of the intermediate step for stabilization, often required for pyrolysis oil upgrade. Results were in accordance to that of Bridgwater, who reported that no intermediate step for stabilization is required for the oils, obtained in direct liquefaction [7], as the upgraded product had low viscosity and the same rheological properties as

the oils, obtained at the lower heat-up rates by using the same catalyst types.

Fig. 7c represents the catalyst with the highest active metal loadings and the highest specific surface area. It actually exhibited the greatest activity for the hydrocracking (for both methane and propane) and decarboxylation among NiMo catalysts, while decarbonylation was inhibited and its rate being among the lowest. Final hydroxyl group conversion was slightly lower in comparison to NiMo #1 and NiMo #2 catalyst that is the values of the extents of reactions were close. However, considering intermediate OH concentrations, deoxygenation rate was greater in the initial stages of reactions. Fig. 7d represents the results for NiMo #4 that had the lowest metal loading and the lowest specific surface area. Hydrocracking was among the least expressed, while CO$_2$ formation was comparable to NiMo #2 and higher than NiMo #1. Hydroxyl group conversion was a lot lower than for any other sulphide-form NiMo/Al$_2$O$_3$ catalysts. To sum up, active metal loadings and specific surface area that are directly connected with the quantity of catalytically active centres had a great influence on the rate of hydroxyl group removal and hydrocracking reactions. Any trend regarding decarbonylation and decarboxylation
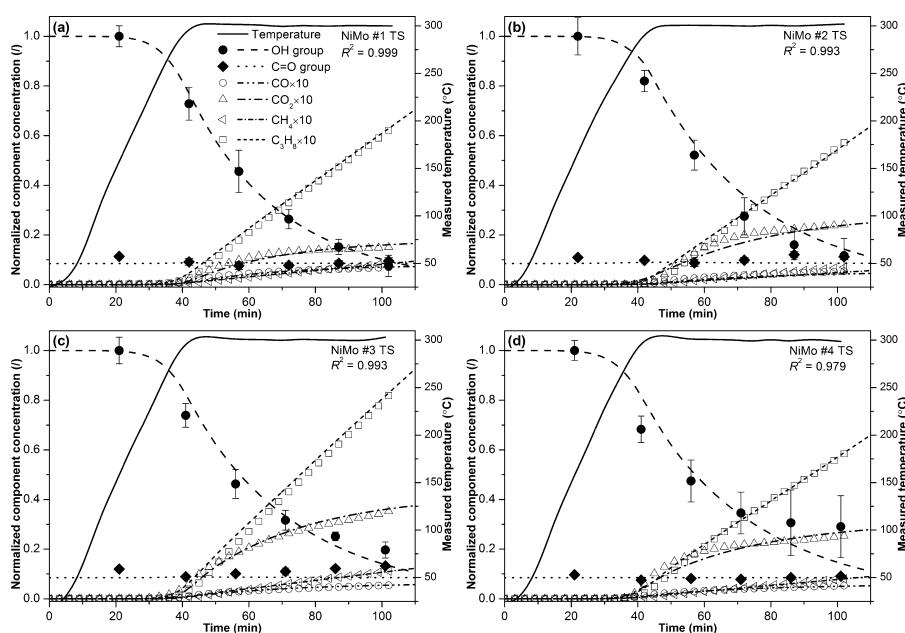

Fig. 7. Experimental (symbols) and modelling (lines) results of hydrotreatment using sulphide-form NiMo/Al$_2$O$_3$ catalysts: NiMo #1 TS (a), NiMo #2 TS (b), NiMo #3 TS (c), and NiMo #4 TS (d); all experiments were performed at the same conditions: temperature of 300 °C, heat-up rate of 7.5 K min^{-1}, total pressure of 8 MPa, stirring speed of 1000 min^{-1}, 25 wt% of tetralin per mass of liquid phase, and 7.5 wt% of catalyst per mass of primary oil; values of normalized gas concentrations (CO$_2$, CO, CH$_4$ and C$_3$H$_8$) have been multiplied by factor of 10 to grant better clarity in given scale; legend in Fig. 7a refers to all subfigures.
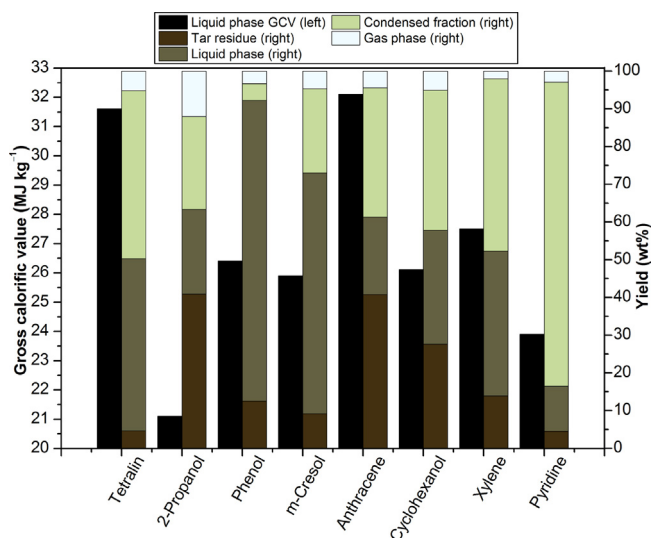
Fig. 8. Effect of hydrogen donor solvents on gross calorific value of liquid phase and fraction yields of hydrotreated primary oil (300 °C, 2.5 K min^{-1}, 8 MPa H$_2$, 1000 min^{-1}, 25 wt% of tetralin per mass of liquid, and 7.5 wt% of catalyst per mass of oil).

reactions was not that straightforward, as they can also occur in a rather large extent by non-catalytic mechanisms.

3.4. Influence of hydrogen donor solvent

Fig. 8 indicates that the solvents, which were examined, showed various effects on the GCV and composition of product using the NiMo #1 in oxide form. GCV was determined for samples, which included solvents; therefore the extent of HDO cannot be directly evaluated by comparing GCV. As expected, tetralin showed the best results regarding a high calorific value and the lowest presence of tarry residues. Tetralin is known to readily dehydrogenate under the conditions of hydrotreatment to yield naphthalene and free hydrogen radicals [41]. The latter promote hydrogenation reactions and stabilize the thermally cleaved free radicals in feedstock, which also seek stabilization among the competing possibilities, and can lead into the tar and char formation in the case of the insufficient availability of the hydrogen radicals in reaction mixture. Naphthalene can be readily hydrogenated back to tetralin in the presence of molecular hydrogen and is stable within HDO temperature range [39].

The use of 2-propanol, on the other hand, resulted in an extensive formation of char, visually very similar to carbon black with GCV of 19.5 MJ kg^{-1}. The GCV of liquid product was the lowest among solvents, which were tested, while the yield of gas phase was the highest, probably due to the thermal decomposition and hydrodeoxygenation of solvent itself, as a very high content of propane was detected in gas phase. Obviously, 2-propanol could neither stabilize the thermally cleaved fragments in feedstock nor contribute to the hydrogenation and hydrogenolysis with hydrogen transfer. Furthermore, the hydroxyl group from propanol might act as the agent for liquefaction and react with the incompletely solvated macromolecules in primary oil. The mechanism of propanol reacting as hydrogen donor solvent might require alkaline reaction medium [24]. The use of anthracene resulted in the highest calorific value of liquid phase, but also in the highest viscosity and tar residue content that is re-polymerisation reactions were evidently favoured. The condensed fraction in this run had the GCV of 11.4 MJ kg^{-1}. The hydrogen transfer mechanism of anthracene should be analogous to that of tetralin, where the ring of anthracene

would be saturated by the hydrogenation in the first step, followed by the thermal process of re-aromatisation, yielding 4 hydrogen radicals. Mass balance was similar to the one, obtained upon the use of tetralin, except for high tar content that might also reflect the high pour point of anthracene by itself. On the other hand, pyridine seemed to enhance hydrocracking reactions, as more than 80 wt% of feedstock was transformed into volatile form that condensed in water-cooled condenser, and had the GCV of 23.2 MJ kg^{-1}.

The addition of phenol, *m*-cresol, cyclohexanol, and xylene resulted in comparable GCV (26.7 ± 1 MJ kg^{-1}) and the viscosity of liquid phase, while tarry residue was below 14 wt% except for cyclohexanol (28 wt%). The run with xylene reveals that it does not possess considerable hydrogen donor activity, as the GCV of liquid product is significantly lower in comparison to the tests with other aromatic hydrocarbons, e.g. anthracene and tetralin. By using phenol, over 80 wt% of liquid phase yield and a low amount of tarry residue indicated extraordinary radical stabilization, while liquid phase GCV was still unacceptably low; consequently, HDO reactions were not promoted in a desired extent. However, the high yields and low amount of tarry residue shows some potential for phenol to be used as hydrogen donor solvent, so that the further investigations with more active (e.g. sulphided) catalysts would be required. In summary, tetralin showed the superior hydrogen donor properties at investigated reaction conditions, as very low tar residue amount was present and viscosity was among the lowest. Among used solvents, only phenol and partly cresol showed the potential applicability for the substitution of tetralin, the latter being rather expensive, as hydrogen donor solvent.

4. Conclusions

This work presents a catalyst and hydrogen donor solvent screening study for the hydrotreatment of the solvolytic primary oil, obtained with the low-temperature liquefaction of lignocellulosic biomass waste. Reactions were carried out in a batch reactor (slurry) with the constant flow of the fresh hydrogen at 300 °C and 8 MPa. Distinct differences between the catalysts, their pre-treatment method, and hydrogen donor solvent addition on product yield, GCV, activity, and selectivity were observed. Among the studied catalysts, the sulphide-form of commercially available NiMo/Al$_2$O$_3$ catalysts resulted in the most suitable liquid product, regarding yield, rheological properties, and high GCV, while the highest GCV of liquid phase was obtained by the oxide form of NiMo catalyst. The palladium catalysts on alumina and carbon supports showed only low catalytic activity and are commercially less acceptable also due to their high price. Bulk MoS$_2$ catalysts, on the other hand, are promising, because of their low price, relatively high activity, and HDO selectivity, and should be further investigated in the future. Among the solvents, which were tested, tetralin entitled the reputation of the effective hydrogen donor solvent both in terms of successful radical stabilization, and in enhancing hydrogenation and hydrogenolysis reactions.

Appendix A. Supplementary data

Supplementary data associated with this article can be found, in the online version, at http://dx.doi.org/10.1016/j.apcatb.2013.12.030.

References

[1] M.F. Demirbas, M. Balat, Energy Convers. Manage. 47 (2006) 2371–2381.
[2] H.R. Appell, Y.C. Fu, S. Friedman, P.M. Yavorsky, I. Wender, Converting Organic Wastes to Oil; a Replenishable Energy Source, Report of Investigation 7560, Pittsburgh Energy Research Center, US Dept. of the Interior, Pittsburgh, PA, 1971.
[3] F. Behrendt, Y. Neubauer, M. Oevermann, B. Wilmes, N. Zobel, Chem. Eng. Technol. 31 (2008) 667–677.
[4] A. Kržan, E. Žagar, Bioresour. Technol. 100 (2009) 3143–3146.
[5] S.-A. Rezzoug, R. Capart, Biomass Bioenerg. 11 (1996) 343–352.
[6] A. Demirbas, Energy Convers. Manage. 41 (2000) 1741–1748.
[7] A.V. Bridgwater, Appl. Catal. A: Gen. 116 (1994) 5–47.
[8] P.M. Mortensen, J.D. Grunwaldt, P.A. Jensen, K.G. Knudsen, A.D. Jensen, Appl. Catal. A: Gen. 407 (2011) 1–19.
[9] E. Furimsky, Appl. Catal. A: Gen. 199 (2000) 147–190.
[10] D.C. Elliott, Energy Fuels 21 (2007) 1792–1815.
[11] S.-A. Rezzoug, R. Capart, Appl. Energy 72 (2002) 631–644.
[12] X. Wang, R.Y. Saleh, U.S. Ozkan, Appl. Catal. A: Gen. 286 (2005) 111–119.
[13] L. Chen, Y. Zhu, H. Zheng, C. Zhang, B. Zhang, Y. Li, J. Mol. Catal. A: Chem. 351 (2011) 217–227.
[14] B. Donnis, R. Egeberg, P. Blom, K. Knudsen, Top. Catal. 52 (2009) 229–240.
[15] Y. Romero, F. Richard, S. Brunet, Appl. Catal. B: Environ. 98 (2010) 213–223.
[16] M.V. Bykova, D.Y. Ermakov, V.V. Kaichev, O.A. Bulavchenko, A.A. Saraev, M.Y. Lebedev, V.A. Yakovlev, Appl. Catal. B: Environ. 113–114 (2012) 296–307.
[17] R. Olcese, M.M. Bettahar, B. Malaman, J. Ghanbaja, L. Tibavizco, D. Petitjean, A. Dufour, Appl. Catal. B: Environ. 129 (2013) 528–538.
[18] X. Zhang, Q. Zhang, T. Wang, L. Ma, Y. Yu, L. Chen, Bioresour. Technol. 134 (2013) 73–80.
[19] A.R. Ardiyanti, A. Gutierrez, M.L. Honkela, A.O.I. Krause, H.J. Heeres, Appl. Catal. A: Gen. 407 (2011) 56–66.
[20] J. Wildschut, F.H. Mahfud, R.H. Venderbosch, H.J. Heeres, Ind. Eng. Chem. Res. 48 (2009) 10324–10334.
[21] T.V. Choudhary, C.B. Phillips, Appl. Catal. A: Gen. 397 (2011) 1–12.
[22] J.M. Moffatt, R.P. Overend, Biomass 7 (1985) 99–123.
[23] E. Churin, P. Grange, B. Delmon, Quality Improvement of Pyrolysis Oils, Final Report Volume 12441, Commission of the European Communities, Luxembourg, 1989.
[24] N.P. Vasilakos, D.M. Austgen, Ind. Eng. Chem. Proc. Des. Dev. 24 (1985) 304–311.
[25] S.P. Zhang, Y.J. Yan, Z. Ren, T. Li, Energy Source 25 (2003) 57–65.
[26] Y.-H.E. Sheu, R.G. Anthony, E.J. Soltes, Fuel Process. Technol. 19 (1988) 31–50.
[27] M. Grilc, B. Likozar, J. Levec, Biomass Bioenerg. 57 (2013) 1–37.
[28] T. Seljak, S. Rodman Oprešnik, M. Kunaver, T. Katrašnik, Appl. Energy 99 (2012) 40–49.
[29] M. Kunaver, E. Jasiukaitytė, N. Čuk, Bioresour. Technol. 103 (2012) 360–366.
[30] J. Zakzeski, R.J.H. Grisel, A.T. Smit, B.M. Weckhuysen, ChemSusChem 5 (2012) 430–437.
[31] S.G.A. Ferraz, F.M.Z. Zotin, L.R.R. Araujo, J.L. Zotin, Appl. Catal. A: Gen. 384 (2010) 51–57.
[32] P.K. Kanaujia, Y.K. Sharma, U.C. Agrawal, M.O. Garg, Trends Anal. Chem. 42 (2013) 125–136.
[33] N. Li, G.W. Huber, J. Catal. 270 (2010) 48–59.
[34] A. Wawrzetz, B. Peng, A. Hrabar, A. Jentys, A.A. Lemonidou, J.A. Lercher, J. Catal. 269 (2010) 411–420.
[35] O.İ. Şenol, E.M. Ryymin, T.R. Viljava, A.O.I. Krause, J. Mol. Catal. A: Chem. 268 (2007) 1–8.
[36] F. Budija, C. Tavzes, L. Zupancic-Kralj, M. Petric, Bioresour. Technol. 100 (2009) 3316–3323.
[37] T. Yamada, H. Ono, J. Wood Sci. 47 (2001) 458–464.
[38] J. Sonnemans, P. Mars, J. Catal. 34 (1974) 215–229.
[39] R.J. Hooper, H.A.J. Battaerd, D.G. Evans, Fuel 58 (1979) 132–138.
[40] M. Ruinart de Brimont, C. Dupont, A. Daudin, C. Geantet, P. Raybaud, J. Catal. 286 (2012) 153–164.
[41] G.P. Curran, R.T. Struck, E. Gorin, Ind. Eng. Chem. Process Design Dev. 6 (1967) 166–173.